1-1-2018

Porous Zr2SC-carbon composite microspheres: Possible radiation tolerant sorbents and transmutation hosts for technetium-99

Nicholas Scales
ANSTO, ns112@uowmail.edu.au

Jun Chen
University of Wollongong, junc@uow.edu.au

Robert Aughterson
ANSTO

Inna Karatchevtseva
ANSTO

Attila Stopic
ANSTO

See next page for additional authors

Porous Zr2SC-carbon composite microspheres: Possible radiation tolerant sorbents and transmutation hosts for technetium-99

Abstract

The preparation, characteristics and adsorption properties of novel porous carbon-ceramic composite microspheres are presented. The composites were synthesised by a simple ion exchange process involving the cationic Zr tetramer and commonly-available macroporous sulphonated polystyrene-divinylbenzene cation exchange resins, with subsequent carbothermal reduction at 1350 °C. The materials were extensively characterised with respect to composition, chemical structure and porosity. Carbothermal reduction of the Zr-loaded templates resulted in formation of crystallites of the MAX phase zirconium sulphide carbide (Zr 2 SC) embedded within a highly microporous carbon framework with a macroporous secondary structure inherited from the resin template. Despite the high BET surface areas of the Zr 2 SC-carbon composite microspheres (in some cases, greater than 600 m 2 g −1), they are extremely mechanically robust. The microspheres displayed high adsorption selectivity for oxoanions relative to cationic solution species, including perrhenate (ReO 4 −), a pertechnetate (TcO 4 −) surrogate. Accumulation of ReO 4 − on the Zr 2 SC particles was unequivocally demonstrated by elemental mapping. Such materials are potential candidates as combined 99 Tc sorbents and reusable transmutation hosts.

Disciplines

Engineering | Physical Sciences and Mathematics

Publication Details

Scales, N., Chen, J., Aughterson, R. D., Karatchevtseva, I., Stopic, A., Lumpkin, G. R. & Luca, V. (2018). Porous Zr2SC-carbon composite microspheres: Possible radiation tolerant sorbents and transmutation hosts for technetium-99. Microporous and Mesoporous Materials, 259 67-78.

Authors

Nicholas Scales, Jun Chen, Robert Aughterson, Inna Karatchevtseva, Attila Stopic, Gregory R. Lumpkin, and Vittorio Luca

Porous Zr_2SC-carbon composite microspheres: possible radiation tolerant sorbents and transmutation hosts for technetium-99

Nicholas Scales[a, *], Jun Chen[b], Robert D. Aughterson[a], Inna Karatchevtseva[a], Attila Stopic[a], Gregory R. Lumpkin[a] and Vittorio Luca[c, *]

[a]Australian Nuclear Science and Technology Organisation, Locked Bag 2001, Kirrawee DC, New South Wales, 2232, Australia

[b]Intelligent Polymer Research Institute, ARC Centre of Excellence for Electromaterials Science, Australian Institute of Innovative Materials, University of Wollongong, Innovation Campus, North Wollongong, NSW 2522, Australia

[c]Programa Nacional de Gestión de Residuos Radiactivos, Comisión Nacional de Energía Atómica, Centro Atómico Constituyentes, Av. General, Paz 1499, 1650 San Martin, Provincia de Buenos Aires, República Argentina

[*]Corresponding authors (nsz@ansto.gov.au; vluca@cnea.gov.ar)

Abstract

The preparation, characteristics and adsorption properties of novel porous carbon-ceramic composite microspheres are presented. The composites were synthesised by a simple ion exchange process involving the cationic Zr tetramer and commonly-available macroporous sulphonated polystyrene-divinylbenzene cation exchange resins, with subsequent carbothermal reduction at 1350 °C. The materials were extensively characterised with respect to composition, chemical structure and porosity. Carbothermal reduction of the Zr-loaded templates resulted in formation of crystallites of the MAX phase zirconium sulphide carbide (Zr_2SC) embedded within a highly microporous carbon framework with a macroporous

secondary structure inherited from the resin template. Despite the high BET surface areas of the Zr_2SC-carbon composite microspheres (in some cases, greater than 600 $m^2\ g^{-1}$), they are extremely mechanically robust. The microspheres displayed high adsorption selectivity for oxoanions relative to cationic solution species, including perrhenate (ReO_4^-), a pertechnetate (TcO_4^-) surrogate. Accumulation of ReO_4^- on the Zr_2SC particles was unequivocally demonstrated by elemental mapping. Such materials are potential candidates as combined ^{99}Tc sorbents and reusable transmutation hosts.

Keywords: technetium; adsorption; MAX phase; carbonization; ion exchange resin

1 Introduction

Nuclear power generation has produced as by-products, large inventories of fissile and burnable extremely long-lived isotopes of the transuranic elements (Np, Pu, Am and Cm) as well as long-lived fission products, including, but not limited to, ^{99}Tc, ^{93}Zr, ^{135}Cs, ^{107}Pd and ^{129}I) [1, 2]. The above mentioned transuranics together are responsible for long-term decay heat generation and radiotoxicity. Along with waste partitioning, one means of reducing waste volume and long-term radiotoxicity that has been receiving serious consideration, is transmutation via neutron irradiation, in order to convert long-lived radionuclides into much shorter-lived ones. With respect to the latter initiative, the Gen IV International Forum has selected next-generation reactor types for further R&D, with a goal of a closed nuclear fuel cycle incorporating total actinide burn-up [3]. The irradiation matrix is often conceived as a radiation-tolerant ceramic phase incorporating the Minor Actinides (Np, Am, Cm) in a solid solution or mixture in the form of a fully-dense monolith, *viz.*, Inert Matrix Fuel (IMF). The demands on a host matrix in terms of materials properties can best be described as extreme

and include very high melting point, thermal conductivity, chemical and radiation stability as well as low neutron cross-section. Candidate host matrices include oxide, nitride and carbide ceramics, as well as other mineral-based structures such as $Y_3Al_2O_5$ (yttrium aluminium garnet or YAG) and spinel ($MgSi_2O_4$) [4]. For instance in the ECRIX-H experiment utilising an Am-containing MgO matrix, a transmutation rate of 95% was achieved following irradiation in the Phénix reactor with 29% fast flux for 318 effective full power days [5]. Nevertheless many technical challenges need to be overcome before Minor Actinide transmutation can be implemented. Of the long-lived fission products, the transmutation of ^{99}Tc, ($^{99}Tc + n \rightarrow {}^{100}Ru + \beta^-$) is generally considered technically feasible, although it has received much less attention [1, 6]. The current work attempts to address target materials for the transmutation of ^{99}Tc.

Conventional IMFs are dense single- or two-phase monolithic materials. A single phase system would consist of the radionuclide to be transmuted being incorporated substitutionally within the crystal structure of a ceramic phase. In two-phase systems such as ceramic-ceramic (cercer) or cermic-metallic (cermet) composites the radionuclide is incorporated within a separate phase. For instance, the ECRIX matrices are cercers since they initially consist of $AmO_{1.62}$ particles dispersed in MgO [5]. However, most nuclear fuels have limited burn-up capabilities, and only a fraction (say up to 30%) of the transuranics can be burned before the fuel reaches its damage limits and needs to be reprocessed and refabricated. Therefore reprocessability is an important criterion in determining the utility of a transmutation matrix or fuel. In contrast, wasteform matrices for the immobilization of transuranics are required be extremely insoluble under a wide range of potential geological conditions.

As an alternative to fully-dense transmutation targets, the dissolution of which might be difficult, we suggested in our previous work that the aforementioned candidate host materials

prepared in suitable porous forms could be the basis for radiation-tolerant and reusable targets, but with generation of less solid waste [7]. Porous monoliths would have several potential advantages. First, fission gas generation would be less likely to cause swelling and cracking since the gas could easily be accommodated within pores. Second, high energy fragments resulting from neutronic reactions would always reside near pores. Third, the reactants and products could be introduced and removed by simple solid-liquid phase adsorption and desorption, respectively; and if the materials were prepared in granular forms, could readily lend themselves to column chromatography. Such materials might also find application in the production of nuclear medicines, wherein the easy recycling of costly isotopically-enriched target elements would be desirable to minimise production costs. To this end, we had produced carbon-zirconium carbide composite porous monoliths based on a porous polyacrylonitrile (PAN) sphere template, with demonstrated reversible adsorption of Mo. As one member of the aforementioned candidate transmutation matrices, zirconium carbide (ZrC_{1-x}) possesses excellent thermal conductivity, radiation tolerance and thermal stability [8].

Sorbents for ^{99}Tc have generally included diverse materials such activated carbon, natural minerals, synthetic inorganics and ion exchange resins [9-22]. Metal-Organic Frameworks (MOFs) have also been highlighted for their potential for ^{99}Tc removal and sequestration [23-26]. There have been few examples of porous granular materials for ^{99}Tc capture and especially ones well-suited to demanding radiation environments [27]. However, recently Shu and co-workers reported ion-imprinted inorganic-based magnetic microspheres exhibiting selectivity for ReO_4^- ($^{99}TcO_4^-$ surrogate) even in moderately acidic conditions [28].

The $M_{n+1}AX_n$ (MAX) phases are a relatively new family of layered, machinable, ternary carbides and nitrides; where M is an early transition metal; *A* is one of the elements in groups

13–16; and *X* is C and/or N [29, 30]. Due to their oxidation resistance and other properties there has been considerable interest in their potential as nuclear structural materials. They are normally prepared at high temperatures under reducing conditions and are usually obtained as dense monoliths of little use as adsorbents. However, it has been demonstrated that exfoliation of the MAX phases can yield two-dimensional MXenes (analogous to graphene) with cation intercalation properties [31, 32]. In this work, we report new porous composites containing the Zr_2SC MAX phase, which were fabricated by a straightforward ion exchange-based procedure promoting intimate contact between cationic Zr and polymeric organic cation exchange resins. The latter serve as both porous structural templates and reactive carbon sources, for *in situ* carbide formation via carbothermal reduction. Although metal-loaded ion exchange resins have been employed as precursors for a diverse range of carbon composites with ceramics and metals [33-44], to date this synthetic strategy has only been applied to produce carbides of U and Si [45, 46].

The objective of the current work was to produce novel porous microspheres, which could conceivably be utilised as radiation-tolerant sorbents for the selective capture of ^{99}Tc and its subsequent transmutation. We detail the synthesis of these materials; determine their compositions as well as their chemical and physical structural characteristics; and investigate their adsorption properties.

2 Experimental

2.1 Materials

All chemical reagents including strong cation exchange resins were used as received without further purification. Dowex® DR-2030 H, Amberlyst® 15 H, Dowex® 50WX2 H and Amberlite® IR120 H and $ZrOCl_2.8H_2O$ (98%) were sourced from Sigma Aldrich, Australia. Duolite® C 255 H was obtained from Dia-prosim Limited, UK, while $NaReO_4$ (99.9%) was obtained from Strem Chemicals, USA. Trace metal analytical grade 69% HNO_3 was sourced from Seastar Chemicals Inc, Canada and Merck, Australia; and analytical grade 50 wt% NaOH solution was procured from Fluka Chemicals, Australia. A custom multi-element standard (2% HNO_3 matrix, > 99.96% purity) was supplied by High Purity Standards, USA. This solution was 10 mg L^{-1} with respect to each element and included Al, As, Ba, Be, B, Cd, Ca, Ce, Cs, Cr, Co, Cu, Dy, Er, Eu, Gd, Ga, Ho, Fe, La, Pb, Lu, Mg, Mn, Nd, Ni, P, K, Pr, Re, Rb, Sm, Se, Na, Sr, Tl, Tm, U, V, Yb and Zn. Instrument-grade air and 3.5 mol% H_2 in Ar gas mix were both produced by Coregas, Australia. Milli-Q® water (18.2 MΩ.cm) was used in all experiments.

2.2 Synthesis

2.2.1 Nomenclature

Zirconium-loaded resins were named ZrCX-1 to -5 to indicate the substrates used; these were: macroporous resins Dowex® DR-2030 and Amberlyst® 15 (ZrCX-1 and -2, respectively) and gel resins Dowex® 50WX2, Amberlite® IR-120 and Duolite® C255 (ZrCX-

3 to -5, respectively). Substrates were all sulphonated polystyrene-divinylbenzene strong cation exchange resins (more specifications are given in Table S1).

2.2.2 Zr adsorption

Resins were loaded with aqueous $ZrOCl_2$ solutions using a batch contact time of one day and mild agitation provided by a platform shaker (IKA, Germany). Macroporous resins were loaded with volume-to-mass ratio (V/m) of 50 mL g^{-1} and 0.042 mol L^{-1} $ZrOCl_2$, while for gel resins, V/m of 1 mL g^{-1} and 2.8 mol L^{-1} $ZrOCl_2$ were used. Loaded resins were collected under suction, washed with Milli-Q® water and leached for one day to remove un-adsorbed Zr. The leached resins were re-rinsed, air-dried overnight under suction and vacuum-dried overnight at 60 °C (Thermo Electron, Germany).

2.2.3 Thermal treatment

Detailed conditions for carbothermal reduction were described in our previous work [7]. Briefly, the samples were heated in a graphite boat with lid in an alumina tube furnace under a flow of 3.5 mol% H_2 in Ar mix and 24 hour residence time at any specified temperature. Heat treatment at 1350 °C, being the maximum temperature achievable by the tube furnace, was the standard procedure. Sample codes denote the 1350 °C-heated materials, unless explicitly stated otherwise.

2.3 Characterisation

Thermogravimetric analysis (TGA) of samples (vacuum-dried overnight at 100 °C) was conducted with a Seiko Instruments Inc. EXSTAR6000 thermal analyser under instrument air carrier. Optical images were obtained with a Wild M400 optical macroscope. Secondary

electron images of microsphere fractured surfaces (2–3 nm Pt coated) were acquired with a Zeiss Ultra Plus Scanning Electron Microscope (SEM). Scanning Transmission Electron Microscopy (STEM) images and Energy Dispersive Spectroscopy (EDS) spectra were acquired using a JEOL 2200FS operated at 200 keV. STEM specimens consisted of crushed grains mixed with ethanol and dispersed on holey carbon films supported on TEM Cu mesh grids. Nitrogen adsorption-desorption isotherms of samples (vacuum-degassed at 150 °C) were acquired at 77 K (−196 °C) on a Micromeritics ASAP 2020 instrument. Mercury intrusion profiles were obtained with a Micromeritics Autosorb IV 9520 Mercury Porosimeter. Total surface areas were calculated with the Brunauer-Emmett-Teller (BET) equation; micropore and external surface areas using a t-plot method; and pore size distributions with a Density Functional Theory (DFT), N_2 on carbon slit pore model. Powder X-Ray Diffraction (XRD) patterns were acquired with a PANalytical X'pert Pro X-Ray Diffractometer using Cu weighted Kα radiation 1.5406 / 1.5444 Å 2:1, a step size of 0.0334 °2θ and an effective scan step time of 624.965 s. Rietveld Analysis of Zr_2SC was performed using Rietica software (Version 2.1), employing a Newton-Raphson refinement strategy. Profile fitting was conducted with a pseudo-Voigt function, while backgrounds were fitted with a fifth order polynomial function. For Neutron Activation Analysis (NAA), neutron irradiation was conducted at the OPAL Research Reactor, Lucas Heights, Australia, in a thermal neutron flux of 2.2×10^{13} cm^{-2} s^{-1} for five minutes. Gamma spectra were acquired using high purity Ge gamma detectors (P-type, 25% relative efficiency). Standardisation was achieved using the k_0-method and certified gold wires standards [47]. Microanalysis of O content was performed using a routine inert gas fusion method and employing a LECO TCH600 instrument. All samples for NAA and O microanalysis were first vacuum-dried overnight at 100 °C and vials backfilled with N_2. Raman spectra were collected using a Renishaw inVia Raman spectrometer equipped with a Peltier-cooled CCD detector and set up

with either argon (514 nm) or HeCd (325 nm) laser excitation. The carbon in-plane crystallite size was calculated using a general expression (Eq. 1) taking into account the laser wavelength:

$$L_a = (2.4 \times 10^{-10})\lambda_{laser}^4 \left(\frac{I_D}{I_G}\right)^{-1} \quad (1)$$

where L_a is the in-plane crystallite size (nm), λ_{laser} is the laser wavelength (nm), I_D is the D peak intensity and I_G is the G peak intensity [48]. Individual whole microspheres were mechanically tested between two metal flats (load cell and stationary surface) using an Instron 5967 instrument with 500 N load cell, employing a compression rate of 0.01 mm min^{-1}.

2.4 Adsorption studies

2.4.1 Solution preparation

For a pH 2 elemental selectivity profile, a 0.1 mg L^{-1} cocktail (with respect to each element) was produced by diluting a multi-element custom standard 100-fold into pH 2.5 nitric acid solution, with pH adjustment carried out by addition of aqueous HNO_3, employing magnetic stirring.

For pH dependence studies, a solution 10 mg L^{-1} with respect to Re was produced by dissolution of $NaReO_4$ in Milli-Q® water. With vigorous magnetic stirring, this was pH adjusted with aqueous HNO_3 or NaOH solutions to produce subsamples of various pH values. Each solution was aged for a day and its final pH measured.

For Re capacity measurements, STEM-EDS studies of Re loading and temperature dependence, a 25 mg L^{-1} Re solution was produced by dissolution of $NaReO_4$ in Milli-Q®

200 water, with adjustment to pH 5 with dilute aqueous HNO_3 and employing magnetic stirring.
201 Aged overnight, the pH change was negligible. For kinetics and reuse, 1 mg L^{-1} (pH 5) and
202 10 mg L^{-1} (pH 3) Re solutions, respectively, were prepared similarly.

203 **2.4.2 Contact experiments**

204 Batch contact was conducted at about 20 °C with gentle agitation provided by a platform
205 shaker (IKA, Germany), except for temperature dependence measurements, which were
206 performed in a temperature-controlled shaker oven (WTC Binder, Germany).

207 The pH 2 selectivity survey was performed in triplicate at volume-to-mass ratio (*V*/*m*) of 200
208 mL g^{-1} with a contact time of one day. Supernatants were filtered through hydrophilic 0.45
209 μm syringe filters (Sartorius). Measurements of pH dependence were performed similarly,
210 but with a contact time of three days.

211 For capacity measurements, single solid portions were contacted for four days, with *V*/*m*
212 varied between 50 and 1000 mL g^{-1}. Subsampling of supernatants was conducted by pipette.
213 Re-loading of pre-ground STEM-EDS specimen was executed similarly, but with *V*/*m* of
214 2000 mL g^{-1}.

215 Kinetics measurements were performed in triplicate at *V*/*m* of 200 mL g^{-1}, with time varied
216 between 15 minutes and four days. Supernatants were subsampled by pipette.

217 For reuse studies, adsorption-desorption cycling was effected by changes in HNO_3
218 concentration. A single solid portion was contacted with 10 mg L^{-1} Re solution (pH 3) at *V*/*m*
219 of 200 mL g^{-1} for four days, with subsampling by pipette. The remaining supernatant was
220 removed and replaced with HNO_3 solution (pH 0), with subsequent contact for four days,
221 followed by subsampling by pipette. This procedure was repeated for two full cycles.

Between cycles, the solid material was washed and then leached (V/m of 5000 mL g^{-1}) with Milli-Q® water for three days, to remove residual HNO_3.

Temperature dependence studies were carried out in triplicate with contact at V/m of 200 mL g^{-1} for four days, sequentially at 30, 40 and 50 °C, respectively. Supernatants were removed by pipette and cooled to room temperature prior to dilution for ICP-MS analysis.

Elemental analyses of supernatants and stocks were performed on an Agilent 7900 ICP Mass Spectrometer. Values of % extraction were calculated using Eq. 2:

$$\%\, extraction\ = \frac{C_i - C_e}{C_i} \times 100 \tag{2}$$

and uptakes were calculated with Eq. 3 and 4:

$$q_e = \frac{(C_i - C_e)V}{m} \tag{3}$$

$$q_t = \frac{(C_i - C_t)V}{m} \tag{4}$$

where C_i is initial concentration (mg L^{-1}), C_e is equilibrium concentration (mg L^{-1}), C_t is concentration (mg L^{-1}) at time t, q_e is the equilibrium amount adsorbed (mg g^{-1}), q_t is the amount adsorbed (mg g^{-1}) at time t, V is volume (L) and m is mass of sorbent (g). Triplicates were averaged and errors estimated from two sample standard deviations of each triplicate set.

2.4.3 Model fitting and calculations

Details of standard calculations for fitting adsorption models, as well as thermodynamic calculations, are given in Supplementary Material.

3 Results and Discussion

3.1 Loading of resins

The Zr uptake of the various cation exchange resins exhibited considerable variation. While the macroporous resins (ZrCX-1 and -2 precursors) were readily saturated with dilute $ZrOCl_2$ solution (0.042 mol L^{-1}) (Table S2), loading of the gel resins (ZrCX-3 to -5 precursors) was only satisfactorily achieved with concentrated solutions (2.8 mol L^{-1}). From TGA of the loaded resins (Fig. S1), the refractory residues (presumed to be ZrO_2) were calculated to verify successful loading with Zr. For ZrCX-1 to -5, these were 24.3, 25.0, 28.5, 10.6 and 10.4 wt%, respectively.

3.2 Effect of thermal treatment

Carbothermal reduction products of the Zr-loaded resins at 1350 °C were typically lustrous black and highly spherical microspheres. A typical example, ZrCX-1, is presented in Fig. 1 (images of all materials are supplied in Fig. S2). Upon heating, the specimens exhibited noticeable shrinkage compared to the precursors. The measured BET surface areas for ZrCX-1 to -5 were 609, 626, 401, 7.1 and 7.5 $m^2 g^{-1}$, respectively. Thus, high Zr content seemed to have a positive influence on surface area; the three loaded resins with much higher Zr content (ZrCX-1 to -3) gave very high BET surface areas.

3.3 Composition and chemical structure

Elemental compositions of the thermally-treated microspheres were determined mainly using NAA and supplemented with O microanalysis (Table 1). From NAA, the main constituents were Zr, S, Hf and Na, with the remainder presumed to be mainly C and O. Traces of Cl, Mg, Al, V, Mn, Co and Cs were also found (data not shown). The trends in measured Zr concentrations agreed well with those seen earlier in the TGA of unheated Zr-loaded resins. The presence of Hf was anticipated as it is a common impurity in Zr, due to the difficulty in separating these two elements. The source of Na content was uncertain, however it could indicate that the starting resins were prepared in their Na forms and converted to H forms later on. Considerable O content (4.19–12.7%) was also found. The O in the Zr-loaded precursors originated from both sulphonate ($-SO_3H$) and zirconyl ($[Zr_4(OH)_8]^{8+}$) moieties; the naked polymer frameworks do not contain it. The compositional remainders (42–75.5 wt%), were inferred to be mainly C, making up the porous frameworks and the majority component in four out of the five materials.

Powder XRD patterns for ZrCX-1 to -5 are presented in Fig. 2a. Despite initial expectations of producing ZrC, the three high surface area materials, ZrCX-1 to -3, showed the same distinct reflections of a crystalline phase identified as the MAX phase zirconium sulphide carbide (Zr_2SC) [29, 30]. The Zr_2SC phase is known to have a $P6_3/mmc$ (hexagonal) space group [30]. The other two materials displayed broad irregular shaped bumps which were interpreted as amorphous content or very short-range order. Using Rietveld Analysis, attempts were made at fitting a hexagonal structure model to the data. Fitting background functions proved challenging due to the high background. Use of a beam knife did not improve this situation (data not shown) and it was concluded that the backgrounds was due to amorphous content. Despite this difficulty, peak positions were accurately fitted and lattice

parameters calculated. The a and c cell dimensions (Å) for Zr_2SC in ZrCX-1 to -3 were, respectively: 3.416 ± 0.002, 12.143 ± 0.007; 3.417 ± 0.004, 12.150 ± 0.014; and 3.423 ± 0.013, 12.16 ± 0.04. These agreed well with previously reported values for this particular MAX phase (summarised in Table S3) [49-57]. Interestingly, the Zr-to-S molar ratios calculated from the compositional data above, ranged from 0.9 to 1.3; less than the 2:1 proportions expected from the Zr_2SC formula. The Zr-to-C molar ratios ranged from about 0.02 to 0.1, indicating that C was in vast excess. However, given the close agreement in lattice dimensions to prior examples, a deviation in stoichiometry of the MAX phase seems unlikely.

The carbon phases of ZrCX-1 to -3 were characterised by Raman Spectroscopy. Visible and UV excitation Raman spectra for ZrCX-1 are shown (Fig. 2b); those of the other two materials were highly similar and are given in Fig. S3. First, the absence of a discernible T peak (~ 1060 cm^{-1}) in the 325 nm (UV excitation) spectrum demonstrated that sp^3-hybridised carbon content was insignificant. The G peak (~ 1600 cm^{-1}) was unambiguous evidence of a ringed sp^2 carbon structure. Furthermore, the G peak did not disperse (that is, change of peak position as a function of laser excitation frequency), but only the D peak dispersed; this is seen only in ordered carbons such as graphite, nanocrystalline graphite and glass-like carbon [58]. Thus the carbon component of the composites appears to consist of a well-ordered ringed sp^2 carbon structure, with relatively few defects.

The 2D (overtone) peak provides information about stacking order of sp^2 carbon sheets. In highly-graphitised carbon, a fine structure is observed [48]. This was absent in the 2D peak of the 514 nm spectrum of ZrCX-1, which instead showed a single smooth symmetrical peak. This was thus evidence of disordered stacking or turbostraticity of the carbon sheets similar

304 to the so-called non-graphitic carbons [59]. An equally valid interpretation would be that the
305 sheets were randomly positioned in space, relative to one other.

306 Summarising, while there was evidence of an ordered ringed sp^2 graphene-like motif in
307 ZrCX-1, the carbon matrix exhibited a disordered three-dimensional structure.

308 **3.4 Porosity**

309 The internal pore structures of the materials were investigated with SEM. In the two
310 macroporous resin-derived materials, ZrCX-1 and -2 (Fig. 3a–d), no large macropores (i.e.
311 pores of the order of tens to hundreds of micrometres in diameter) could be observed. At
312 higher magnification, irregular coral-shaped polymer structures were observed in both
313 materials, surrounded by sub-micrometre macropores. Smaller gaps between adjacent
314 branches could be interpreted as mesopores. The gel resin-derived microspheres, ZrCX-3 to -
315 5 (Fig. 3e-j), were also lacking in large macropores, but somewhat smoother surface textures
316 were observed at higher magnification. Thus, these latter materials did not have the small
317 meso- and macropore architectures of the macroporous resin-derived microspheres. While
318 some evident loose surface fragments were noted in two of the images, these were probably
319 artefacts of the sample preparation.

320 The high surface area materials ZrCX-1 to -3 were examined by Nitrogen Porosimetry.
321 Adsorption-desorption isotherms of these materials are presented in Fig. 4a. All three Zr-
322 loaded resins developed considerable microporosity on heating, manifested as low relative
323 pressure branches characteristic of the Type I adsorption isotherm [60]. However, the
324 unloaded parent resins (Dowex® DR-2030, Amberlyst® 15 and Dowex® 50WX2,
325 respectively) upon similar heating, gave much lower surface areas of 25, 59 and < 1 $m^2 g^{-1}$,
326 respectively. This implied that the inorganic portion played a role in the development of

327 microporosity and also that volatilisation of carbonaceous material could be ruled out as a
328 cause. The two macroporous resin-derived materials retained considerable
329 mesoporous/macroporous character of their parents, in contrast to the gel resin, which
330 collapsed on heating to yield a non-porous product whose surface area was too low to
331 accurately measure.

332 While the gel resin-derived ZrCX-3 exhibited a pure Type I isotherm, in ZrCX-1 and ZrCX-2
333 Type IV hysteresis loops were also observed, indicative of mesoporosity [60]. The hystereses
334 displayed reasonably flat plateaux, suggesting complete mesopore filling and the absence of
335 substantial macropore and/or external surface areas which would be manifested as Type II-
336 shaped features at relative pressures approaching unity [60]. The DFT pore size distributions
337 for ZrCX-1 to -3 (Fig. 4b), confirmed a mixture of micro- and large mesopores for both
338 ZrCX-1 and ZrCX-2 and only micropores for ZrCX-3. The former type of hierarchical
339 porosity would be highly desirable in order to facilitate mass transport.

340 Mercury Intrusion Porosimetry of whole microspheres was also undertaken (Fig. S4), but was
341 largely uninformative with respect to macropores. Apart from intrusion of interstitial
342 porosity, only mesopore openings were revealed; this thus demonstrated that the microsphere
343 surfaces were mesoporous.

344 **3.5 Mechanical testing**

345 Compressive strength testing of ZrCX-1 to -5 microspheres was conducted. Material ZrCX-1
346 was exceedingly robust with an average failure point of 38.3 N and sample standard deviation
347 of 6.3 N (n = 10). The microspheres shattered upon failure. A representative profile is given
348 in Fig. S5. The smaller-sized ZrCX-3 behaved similarly, with an average failure point of 24.7
349 N and sample standard deviation of 4.8 N (n = 10). The two low surface area materials also

proved to be mechanically strong and exhibited similar-shaped profiles, but also wide-ranging variation in mechanical strength. ZrCX-4 yielded an average failure point of 26.0 N and sample standard deviation of 19.0 N (n = 12), while ZrCX-5, the most robust of the series, gave an average failure point of 109.7 N and sample standard deviation of 62.3 N (n = 10). However, the compression behaviour for material ZrCX-2 (n = 11) was not reproducible with respect to profile shapes or failure points (data not shown), probably on account of the significant proportion of irregular-shaped microsphere fragments. Based on the brittle (albeit strong) overall nature of the materials and earlier presented Raman data, we would suggest that the carbon frameworks are probably akin to glass-like carbon.

Considering that a typical ZrCX-1 microsphere weighed approximately 0.1 mg, it follows that the same could withstand a compressive force equivalent to approximately 40 million times its own weight (assuming g of 9.81 m s^{-2}). Therefore, mechanical strength should be no limitation for deployment in separation applications, such as in columns, batch contact or fluidised beds. In comparison, Drisko and co-workers produced fairly robust hierarchically porous zirconium titanium oxide beads which could withstand up to 0.57 N [61].

3.6 Structural evolution with temperature

Based on its combination of favourable properties including multi-scale porosity, high surface area and mechanical strength, ZrCX-1 was selected for the further study of its structural evolution with temperature (Fig. 5). From XRD data, a crystalline phase identified as tetragonal ZrO_2 ($tZrO_2$) had formed by 450 °C, which generally grew in intensity with increasing temperature (Fig. S6a). By 1150 °C, the peak intensity of $tZrO_2$ had diminished somewhat and from around 1250 °C, the hexagonal MAX phase Zr_2SC appeared which had increased in intensity by 1350 °C (Fig 5a).

Surface area changes were monitored from 350–1350 °C (Fig. 5b; the complete set of associated adsorption-desorption isotherms are given in Fig. S6b and c). The low external surface areas for all temperatures confirmed that most of the BET surface area was associated with micropore content. While it would be tempting to attribute microporosity to the interstices between crystallites, or between crystallites and the carbon phase, the surface area changes did not always correlate with the appearance or disappearance of the crystalline phases. As examples, at 950 °C a large drop in surface area was seen even though no new crystalline phase had appeared; and at the intermediate stage of 1150 °C, surface area increased dramatically despite the absence of a well-defined crystalline phase. Instead, we postulate that surface area increases were due to the reaction of volatile oxygen with carbon *in situ* and/or voids left in the carbon phase by reaction with the inorganic phases. Conversely, surface area losses were due to consolidation of groups of smaller pores to form larger ones. One might consider this a form of activation, although any O-containing functionalities generated on the carbon surface would likely be removed by the reducing and carburising conditions.

Calculation of carbon in-plane crystallite size, L_a, for 550 – 1350 °C (Fig. 5c) revealed an almost linear downward relationship with temperature. Intuitively, one might expect carbonisation to give the opposite result, that is, coalescence of carbon domains, for example, as displayed by polyacrylonitrile [62]. These observations, however, are consistent with reactive carbon removal (postulated above) giving rise to increasingly tenuous connections between carbon domains and statistically, the semblance of smaller average crystallite sizes.

Taken together, these characterisation data support a hypothesis of micropore generation within the carbon phase. By extension, this explanation probably also accounts for the high

surface areas of the other two MAX phase-containing materials; and the low surfaces of the two materials, ZrCX-4 and -5, in which the Zr_2SC phase did not form.

3.7 Adsorption properties

The adsorption properties of ZrCX-1 were scoped for a large suite of 41 elements at pH 2 (please refer to § 2.1 Materials for the full list). The material showed significant extraction only of oxospecies-forming elements, As (94 ± 4%), Se (93 ± 4%), Re (87 ± 7%) and P (> 95%), with no discernible cation adsorption. Both Se and Re exist under these conditions of pH and concentration as oxoanions, although interestingly, As(V) and P(V) are found predominantly as the neutral species, arsenic acid (H_3AsO_4) and phosphoric acid (H_3PO_4) [63, 64].

The adsorption of Re prompted us to consider ^{99}Tc as a credible adsorbate, given the close similarity in chemistry between these two elements. Existing as the mononuclear tetrahedral anionic species, perrhenate (ReO_4^-), Re is analogous to its cousin in Group 7, one period above, Tc, which exists as pertechnetate (TcO_4^-) [64]. Thus, it is often regarded as a surrogate to predict likely affinity for Tc. The adsorption of ReO_4^- as a function of pH was further investigated for both ZrCX-1 as well as a carbon blank produced by heat-treating the Dowex® DR-2030 parent resin in the same way ($S.A._{BET}$ = 25 $m^2\ g^{-1}$) (Fig. 6a). Material ZrCX-1 showed nearly quantitative extraction of ReO_4^- over the range of pH 3–10.5. By way of comparison, the carbon blank only showed weak affinity, with discernible adsorption only over the range of pH 1–5 and a maximum extraction of *ca.* 20% at pH 3. The adsorption capacity of ZrCX-1 for ReO_4^- at pH 5 was also assessed (Fig. 6b). Isotherm model parameters obtained from fitting to the experimental data are presented in Table 2. The

Freundlich model was a poor fit, with significant non-linearity evident in the data. The Langmuir model fit, however, was considerably better. The calculated value of q_{max} (adsorption capacity) for the latter model was a modest 13.85 mg g^{-1} (*ca.* 0.074 mmol g^{-1}), which visually accorded well with the plotted isotherm data. Capacity of the carbon blank was also surveyed at pH 5 for comparison and showed no measurable adsorption, in agreement with the pH dependence discussed above. Since the high carbon micropore surface area of ZrCX-1 was obviously underutilised, one avenue for increasing adsorption capacity could be to activate this carbon surface by sulphonation; load additional Zr; and repeat carbothermal reduction treatment.

The Re adsorption kinetics of ZrCX-1 were investigated (Fig. 6c). Fit parameters for the pseudo-second-order model are presented in Table 3. Overall, the pseudo-second-order model proved to be reasonable fit to the data. The kinetics were found to be be relatively slow, with equilibrium only reached in 48–72 hours. Measured uptake at 24 hours was *ca.* 96% of q_e. These results can probably be attributed to a lack of large macropores which would facilitate fast intraparticle diffusion.

Measurements of temperature dependence of Re adsorption onto ZrCX-1 were undertaken to quantify the associated thermodynamic parameters (Table 4). Increasing temperature had the effect of reducing the K_d value (Fig. S8). Large negative values of ΔH° (enthalpy) and ΔG° (Gibbs free energy) were calculated, clearly implying that the adsorption was an exothermic and spontaneous process. The negative value of ΔS° (entropy) would indicate ordering at the solid surface.

One might find the preceding fairly convincing evidence for the Zr_2SC phase supplying the majority of adsorption sites. However, efforts were made to corroborate this directly by way of microstructural chemical analysis. Elemental mapping of a portion of the Re-loaded ZrCX-

1 material was undertaken using STEM-EDS (Fig. 7). The bright field image of ZrCX-1 (Fig. 6a) exhibited dark inorganic particles suspended on the lighter-shaded carbon phase. Mapping of Zr, S, O and Re elemental distributions (Fig. 7b–e, respectively) demonstrated that these four elements were mainly associated with one another. Thus, this unequivocally demonstrated that ReO_4^- accumulates upon the Zr_2SC aggregates/particles, with no significant adsorption on the carbon phase. With reference to the earlier bulk compositional data, these results also suggest that O and excess S are not associated with the carbon phase; and in addition to the Zr_2SC itself, may be part of a secondary inorganic phase. Due to the very small scale of the STEM specimen, however, it cannot be ruled out that there are pockets of unreacted material within the bulk of the material, rendered inaccessible to the carbothermal treatment by shrinkage of the resin precursor during heating. It is also possible that some O is dissolved within the Zr_2SC lattice. This latter explanation is plausible, given that other studies have shown that very high temperatures are required to completely remove dissolved O from ZrC and HfC powders [65].

The adsorption results presented above, certainly do contrast with most previous studies of MXenes, which typically show cation extraction; adsorption of alkali metals, alkaline earth metals, Pb as well as U, have all been demonstrated [66-68]. It should be noted, however, that Ying and co-workers reported affinity of $Ti_3C_2T_x$ (T = OH or F) for $Cr_2O_7^{2-}$, seemingly attributable to protonated surface hydroxyl groups [69]. We postulate two mechanisms for Re adsorption, which are not necessarily mutually exclusive. The first is a surface electrostatic model involving attraction by regions of negative charge on high-electronegative O bound to the adsorbate, to regions of positive charge on the carbide surface. This is a strong hypothesis, as it should universally explain adsorption of neutral, anionic and cationic oxospecies. We have also, in fact, observed the adsorption of cationic UO_2^{2+} above pH 3, as well as neutral and anionic Mo species (H_2MoO_4, $HMoO_4^-$ and MoO_4^{2-}) (Fig. S7). In a

second scenario, it is conceivable that the “A layer” S terminating at the solid-liquid interface is oxidised and anion-exchangeable by adsorbate molecules. If this second hypothesis is applicable to any degree, one should expect a concomitant release of S into the surrounded solution.

There have been relatively few studies on the neutron irradiation stability of MAX phases [70-77]. Some phases such as the well-studied Ti_3SiC_2 and Ti_3AlC_2 appear to be reasonably tolerant and may be candidate nuclear structural materials. There would seem to be evidence supporting the role of the A layer in accommodating antisite defects, thus aiding in damage recovery over amorphisation [71, 77]. The antisite formation energies are in turn, influenced by the bonding overlap in the MX layer [71, 73]. The specific performance of Zr_2SC in these respects is unknown. A further consideration is that the cited studies focus on changes to mechanical properties; as to what influence structural damage (if any) might have on the surface chemistry and observed adsorption properties is a question that remains to be answered. Nonetheless, these previous investigations do hold some promise for the durability of the ZrCX-1 sorbent, subjected to irradiation.

The reusability of ZrCX-1 was studied two complete adsorption-desorption cycles by varying the HNO_3 concentration of the contact solution. For cycle one, 96% adsorption was observed and 76% desorption; for cycle 2, 96% adsorption and 89% desorption. These preliminary results show that the ReO_4^- adsorption is in principle reversible, although additional work will be needed to establish optimal conditions.

4 Conclusions

The synthesis of new mechanically robust and highly porous microsphere composites of carbon and the hexagonal MAX phase Zr_2SC, based on a non-laborious procedure involving the carbothermal reduction of Zr-loaded common strong cation exchange resins has been demonstrated. The Zr loadings achieved varied among the resins and appeared to be an important factor in the development of high surface areas and formation of Zr_2SC, which were observed in one gel resin-derived and both macroporous resin-derived materials. Cell dimensions of this phase determined by Rietveld Method agreed well with prior published examples. It was concluded based on Raman data that the carbon phase consisted of ordered carbon sheets with disordered stacking or random orientation in space. Porosity was investigated in the three high surface area Zr_2SC-containing materials using SEM and Nitrogen Porosimetry. All had developed microporosity, while the two macroporous-resin derived materials additionally contained mesopores and small macropores originating from their substrate resins.

Of the three Zr_2SC-containing materials, ZrCX-1 was chosen for further study based on its combination of favourable properties including high surface area, mechanical strength and multi-scale porosity. For ZrCX-1, trends in crystallisation, surface area and carbon in-plane crystallite size as a function of temperature, together supported a hypothesis of micropore formation occurring within the carbon phase due to reactive carbon removal. This carbon phase is ostensibly a relative of glass-like carbon. This hypothesied mechanism probably also accounts for the high surface areas of the other two MAX-phase materials in the series.

Investigation of ZrCX-1 for adsorption selectivity at pH 2, showed affinity for oxospecies-forming elements, including As, Se, Re and P. Both neutral and anionic species were shown to adsorb, suggesting that an electrostatic interaction must play at least some role. Re was

then used as a surrogate in studies designed to anticipate the performance in extraction of ^{99}Tc, a long-lived fission product in High Level Waste (HLW). Nearly quantitative extraction over the range of pH 3–10.5 was demonstrated, with over 90% extraction observed from pH 2. Elemental mapping employing TEM-EDS confirmed the role of the Zr_2SC MAX phase in the adsorption of ReO_4^-. The Langmuir model provided a superior fit to adsorption isotherm data at pH 5, yielding a q_{max} constant (Langmuir adsorption capacity) of 13.85 mg g^{-1}. A suggestion for further optimising this characteristic was offered. Likewise, adsorption kinetics for ZrCX-1 were modelled by pseudo-second-order model and found to be relatively slow (equilibrium reached in 48–72 hours), suggesting future opportunities for optimisation of pore architecture. Thermodynamic measurements demonstrated that the adsorption process was spontaneous and exothermic. The adsorption was also shown to be reversible, indicating the possibility for recycling of the matrix.

Given the simplicity of their syntheses and porous granular natures affording potential use in a chromatographic column, one might envisage one application being the deployment of the materials for the direct selective extraction of ^{99}Tc from HLW and subsequent transmutation with thermal neutrons. For instance, the microspheres could be packed into a column within a Zr-alloyed housing, for convenient loading of ^{99}Tc, neutron irradiation and post-irradiation elution of products. The microspheres are rigid and not subject to swelling effects, unlike polymeric ion exchange resins and are not likely to be damaged by fission gas build-up. Although radiation tolerance is anticipated, this will need to be evaluated for the Zr_2SC phase to properly gauge practical lifespan in a real recycling scenario. That is to say, while prior radiation damage studies of other MAX phases indicate good general stability for this class of materials, the specific performance of the Zr_2SC MAX phase in high thermal neutron fluxes would need to be addressed if it is to be considered for this application. This is a question we are working towards answering.

538

539 Acknowledgements

540 Materials and equipment access were provided and/or funded by Australian Nuclear Science
541 and Technology Organisation (ANSTO). The authors thank the following ANSTO staff for
542 their contributions: Mr Kerry Cruikshank and Dr Ken Short for maintenance and repair of our
543 tube furnace; Mr Karl Toppler and Mr Tim Nicholls for assistance with mechanical testing
544 equipment; Mr Joel Davis for SEM data; and Dr Yingjie Zhang for Chinese language
545 translations. Mercury Porosimetry was conducted by Particle & Surface Sciences Pty Ltd,
546 NSW, Australia, and O microanalysis was performed by CSIRO Mineral Resources, VIC,
547 Australia; both on a pay-per-sample basis. N.S. is grateful to Dr Katerina Bendak of the
548 Children's Cancer Institute, Kensington, Australia, for German language translations. This
549 research has been conducted with the support of the Australian Government Research
550 Training Program Scholarship. Professor Chen also acknowledges the continuous support
551 from Australian National Fabrication Facility (ANFF).

552

553 Figures captions

554

555 Fig. 1. Optical microscopy image of ZrCX-1.

556 Fig. 2. (a) Powder XRD patterns. Key: h, hexagonal Zr_2SC; and (b) Raman spectra of ZrCX-
557 1, representative of ZrCX-1 to -3.

Fig. 3. SEM images of internal fractured microsphere surfaces at 1,000 and 50,000 × magnification. (a) and (b) ZrCX-1; (c) and (d) ZrCX-2; (e) and (f) ZrCX-3; (g) and (h) ZrCX-4; and (i) and (j) ZrCX-5.

Fig. 4. Nitrogen Porosimetry data. (a) adsorption-desorption isotherms; and (b) pore size distributions.

Fig. 5. Structural evolution of ZrCX-1 with temperature. (a) Powder XRD patterns. Key: t, tetragonal ZrO_2; h, hexagonal Zr_2SC; (b) micropore, external and BET surface areas; and (c) in-plane carbon crystallite sizes.

Fig. 6. Adsorption data. (a) pH dependence for ReO_4^- adsorption onto ZrCX-1 and a carbon blank; (b) isotherm data for ReO_4^- adsorption onto ZrCX-1 at pH 5 with fitted Langmuir and Freundlich models; and (c) kinetics data for ReO_4^- adsorption onto ZrCX-1 at pH 5 with pseudo-second-order model fit.

Fig. 7. STEM studies of Re-loaded ZrCX-1. (a) Bright field image; and corresponding STEM-EDS elemental maps (b–e) of Zr, S, O and Re distributions.

Tables

Table 1. Elemental compositions of ZrCX-1 to -5.

Material	*Zr (wt%)*	*S (wt%)*	*O (wt%)*	*Hf (wt%)*	*Na (wt%)*	*Balance (wt%)*
ZrCX-1	26 ± 2	6.9 ± 0.5	9.9 ± 0.2	0.58 ± 0.04	0.0043 ± 0.0003	57 ± 2
ZrCX-2	26 ± 2	8.0 ± 0.6	10.2 ± 0.2	0.57 ± 0.04	0.0051 ± 0.0004	55 ± 2
ZrCX-3	32 ± 2	12.2 ± 0.9	12.7 ± 0.3	0.75 ± 0.05	0.0179 ± 0.0013	42 ± 3

ZrCX-4	11.4 ± 0.8	8.6 ± 0.7	4.19 ± 0.08	0.27 ± 0.02	0.060 ± 0.004	75.5 ± 1.5
ZrCX-5	12.3 ± 0.9	9.6 ± 0.8	4.48 ± 0.09	0.29 ± 0.02	0.40 ± 0.03	73.0 ± 1.7

575

576

577 Table 2. Isotherm model fit parameters for ReO_4^- adsorption onto ZrCX-1 at pH 5.

Model	q_{max} *(mg* g^{-1}*)*	*b (L* mg^{-1}*)*	*n*	K_f *(mg* g^{-1}*)*	R^2
Langmuir	13.85	1.59			0.993
Freundlich			2.97	6.56	0.949

578

579

580

581 Table 3. Kinetic model fit parameters for ReO_4^- adsorption onto ZrCX-1 at pH 5.

Model	q_e *(mg* g^{-1}*)*	k_2 *(g* $mg^{-1}h^{-1}$*)*	R^2
Pseudo-second-order	0.200	2.36	0.999

582

583

584 Table 4. Thermodynamic parameters for ReO_4^- adsorption onto ZrCX-1 at pH 5.

ΔS° *(J* K^{-1} mol^{-1}*)*	ΔH° *(kJ* mol^{-1}*)*	*Temperature (°C)*	ΔG° *(kJ* mol^{-1}*)*
−109.0	−57.07	30	−24.01

	40	−22.92
	50	−21.83

585

586

587

588

589 ## References

590 [1] K. Kora, H. Nakaya, H. Matsuura, M. Goto, S. Nakagawa, S. Shimakawa, A study on
591 transmutation of LLFPs using various types of HTGRs, Nucl. Eng. Des., 300 (2016) 330-338.
592 [2] B.R. Bergelson, A.S. Gerasimov, G.V. Tikhomirov, Radiotoxicity and decay heat power
593 of spent nuclear fuel of VVER type reactors at long-term storage, Radiat Prot Dosimetry, 115
594 (2005) 445-447.
595 [3] A Technology Roadmap for Generation IV Nuclear Energy Systems, 2002.
596 [4] S. Pillon, Actinide-bearing fuels and transmutation targets, in: R.J.M. Konings (Ed.)
597 Comprehensive Nuclear Materials, Elsevier B.V., 2012, pp. 109-141.
598 [5] J. Lamontagne, Y. Pontillon, E. Esbelin, S. Bejaoui, B. Pasquet, P. Bourdot, J.M.
599 Bonnerot, Determining the americium transmutation rate and fission rate by post-irradiation
600 examination within the scope of the ECRIX-H experiment, J. Nucl. Mater., 440 (2013) 366-
601 376.
602 [6] M. Salvatores, I. Slessarev, A. Tchistiakov, The transmutation of long-lived fission
603 products by neutron irradiation, Nucl. Sci. Eng., 130 (1998) 309-319.
604 [7] N. Scales, J. Chen, T.L. Hanley, D.P. Riley, G.R. Lumpkin, V. Luca, Hierarchically
605 porous carbon-zirconium carbide spheres as potentially reusable transmutation targets,
606 Microporous Mesoporous Mater., 212 (2015) 100-109.
607 [8] Y. Katoh, G. Vasudevamurthy, T. Nozawa, L.L. Snead, Properties of zirconium carbide
608 for nuclear fuel applications, J. Nucl. Mater., 441 (2013) 718-742.
609 [9] B. Gu, K.E. Dowlen, L. Liang, J.L. Clausen, Efficient separation and recovery of
610 technetium-99 from contaminated groundwater, Sep. Technol., 6 (1996) 123-132.
611 [10] E. Holm, T. Gafvert, P. Lindahl, P. Roos, In situ sorption of technetium using activated
612 carbon, Appl. Radiat. Isot., 53 (2000) 153-157.
613 [11] Y.F. Wang, H.Z. Gao, R. Yeredla, H.F. Xu, M. Abrecht, Control of pertechnetate
614 sorption on activated carbon by surface functional groups, Journal of Colloid and Interface
615 Science, 305 (2007) 209-217.

[12] N.N. Popova, G.L. Bykov, G.A. Petukhova, I.G. Tananaev, B.G. Ershov, Sorption of Tc(VII) and Am(III) by carbon materials: effect of oxidation, J. Radioanal. Nucl. Chem., 298 (2013) 1463-1468.
[13] H. Zhuang, J. Zeng, L. Zhu, Sorption of radionuclides technetium and iodine on minerals, Radiochim. Acta, 44-45 (1988) 143-145.
[14] A. Winkler, H. Bruehl, C. Trapp, W.D. Bock, Mobility of technetium in various rocks and defined combinations of natural minerals, Radiochim. Acta, 44-45 (1988) 183-186.
[15] S. El-Wear, K.E. German, V.F. Peretrukhin, Sorption of technetium on inorganic sorbents and natural minerals, J. Radioanal. Nucl. Chem., 157 (1992) 3-14.
[16] L. Liang, B. Gu, X. Yin, Removal of technetium-99 from contaminated groundwater with sorbents and reductive materials, Sep. Technol., 6 (1996) 111-122.
[17] M.J. Kang, S.W. Rhee, H. Moon, V. Neck, T. Fanghaenel, Sorption of MO4- (M = Tc, Re) on Mg/Al layered double hydroxide by anion exchange, Radiochim. Acta, 75 (1996) 169-173.
[18] D.J. Liu, X.H. Fan, Adsorption behavior of 99Tc on Fe, Fe2O3 and Fe2O4, J. Radioanal. Nucl. Chem., 264 (2005) 691-698.
[19] V. Peretroukhine, C. Sergeant, G. Deves, S. Poulain, M.H. Vesvres, B. Thomas, M. Simonoff, Technetium sorption by stibnite from natural water, Radiochim. Acta, 94 (2006) 665-669.
[20] R. Koivula, R. Harjula, Selective sorption of technetium on antimony-doped tin dioxide, Sep. Sci. Technol., 46 (2011) 315-320.
[21] G. Sheng, Y. Tang, W. Linghu, L. Wang, J. Li, H. Li, X. Wang, Y. Huang, Enhanced immobilization of ReO4- by nanoscale zerovalent iron supported on layered double hydroxide via an advanced XAFS approach: Implications for TcO4- sequestration, Appl. Catal., B, 192 (2016) 268-276.
[22] I.E. Burgeson, J.R. Deschane, D.L. Blanchard, Jr., Removal of technetium from Hanford tank waste supernates, Sep. Sci. Technol., 40 (2005) 201-223.
[23] H. Fei, D.L. Rogow, S.R.J. Oliver, Reversible Anion Exchange and Catalytic Properties of Two Cationic Metal-Organic Frameworks Based on Cu(I) and Ag(I), J. Am. Chem. Soc., 132 (2010) 7202-7209.
[24] R. Cao, B.D. McCarthy, S.J. Lippard, Immobilization, Trapping, and Anion Exchange of Perrhenate Ion Using Copper-Based Tripodal Complexes, Inorg. Chem., 50 (2011) 9499-9507.
[25] D. Sheng, L. Zhu, C. Xu, C. Xiao, Y. Wang, Y. Wang, L. Chen, J. Diwu, J. Chen, Z. Chai, T.E. Albrecht-Schmitt, S. Wang, Efficient and Selective Uptake of TcO4- by a Cationic Metal-Organic Framework Material with Open Ag+ Sites, Environ. Sci. Technol., 51 (2017) 3471-3479.
[26] L. Zhu, C. Xiao, X. Dai, J. Li, D. Gui, D. Sheng, L. Chen, R. Zhou, Z. Chai, T.E. Albrecht-Schmitt, S. Wang, Exceptional Perrhenate/Pertechnetate Uptake and Subsequent Immobilization by a Low-Dimensional Cationic Coordination Polymer: Overcoming the Hofmeister Bias Selectivity, Environ. Sci. Technol. Lett., 4 (2017) 316-322.
[27] D. Banerjee, W. Xu, Z. Nie, L.E.V. Johnson, C. Coghlan, M.L. Sushko, D. Kim, M.J. Schweiger, A.A. Kruger, C.J. Doonan, P.K. Thallapally, Zirconium-Based Metal-Organic Framework for Removal of Perrhenate from Water, Inorg. Chem., 55 (2016) 8241-8243.
[28] X. Shu, L. Shen, Y. Wei, D. Hua, Synthesis of surface ion-imprinted magnetic microsphere for efficient sorption of perrhenate: A structural surrogate for pertechnetate, J. Mol. Liq., 211 (2015) 621-627.
[29] H. Nowotny, W. Jeitschko, F. Benesovsky, Novel complex carbides and nitrides and their relation to phases of hard substances, Planseeber. Pulvermetall., 12 (1964) 31-43.

[30] M.W. Barsoum, The MN+1AXN phases: a new class of solids; thermodynamically stable nanolaminates, Prog. Solid State Chem., 28 (2000) 201-281.
[31] M. Naguib, M. Kurtoglu, V. Presser, J. Lu, J. Niu, M. Heon, L. Hultman, Y. Gogotsi, M.W. Barsoum, Two-Dimensional Nanocrystals Produced by Exfoliation of Ti3AlC2, Adv. Mater. (Weinheim, Ger.), 23 (2011) 4248-4253.
[32] M. Naguib, O. Mashtalir, J. Carle, V. Presser, J. Lu, L. Hultman, Y. Gogotsi, M.W. Barsoum, Two-Dimensional Transition Metal Carbides, ACS Nano, 6 (2012) 1322-1331.
[33] K.F. Blurton, Preparation of highly dispersed platinum on carbon, Carbon, 10 (1972) 305-315.
[34] K. Miura, H. Nakagawa, Preparation of metal-loaded porous carbons and their use as a highly active catalyst for reduction of nitric oxide (NO), in: E. Yasuda, M. Inagaki, K. Kaneko, M. Endo, A. Oya, Y. Tanabe (Eds.) Carbon Alloys: Novel Concepts to Develop Carbon Science and Technology, Elsevier Science Ltd., 2003, pp. 499-513.
[35] P. Trens, V. Caps, J.W. Peckett, Catalytic oxidation of trans-stilbene using pyrolysed manganese-loaded cation exchange resin, Appl. Catal., A, 251 (2003) 19-28.
[36] P. Trens, J.W. Peckett, V.N. Stathopoulos, M.J. Hudson, P.J. Pomonis, Phosphotungstate anions supported on spherical beads of carbon as highly efficient catalysts for the dehydration of propan-2-ol to propene, Appl. Catal., A, 241 (2003) 217-226.
[37] B. Li, Y. Ren, Q. Fan, A. Feng, W. Dong, Preparation and characterization of spherical nickel-doped carbonaceous resin as hydrogenation catalysts. I. Carbonization procedures, Carbon, 42 (2004) 2669-2676.
[38] W. Yu, J. Zheng, X. He, Y. Zhao, Synthesis of spherical activated carbon loaded with metal particles and its performance of thiophene adsorption, Huagong Xuebao (Chin. Ed.), 59 (2008) 2824-2829.
[39] W. Yu, Y. Zhang, T. Li, Y. Zhao, X. Qu, Y. Liu, S. Li, Spherical activated carbon material loaded with metal, and preparation method and application thereof, CN101385966A, 2009.
[40] S. Kudo, T. Maki, K. Miura, K. Mae, High porous carbon with Cu/ZnO nanoparticles made by the pyrolysis of carbon material as a catalyst for steam reforming of methanol and dimethyl ether, Carbon, 48 (2010) 1186-1195.
[41] M.S. Wilson, A. Delariva, F.H. Garzon, Synthesis of sub-2 nm ceria crystallites in carbon matrixes by simple pyrolysis of ion-exchange resins, J. Mater. Chem., 21 (2011) 7418-7424.
[42] L. Kotai, T. Pasinszki, Z. Czegeny, S. Balint, I. Sajo, Z. May, P. Nemeth, Z. Karoly, P.K. Sharma, V. Sharma, K.K. Banerji, Metal and metal-sulfide containing carbons from sulfonated styrene-divinylbenzene copolymer based ion-exchangers, Eur. Chem. Bull., 1 (2012) 398-400.
[43] W. Li, Z. Zhang, A. Cui, J. Fan, X. Sun, A gasoline desulfurization adsorbent and preparation method thereof, CN103143321A, 2013.
[44] J. Fan, H. Lan, Z. Zhang, W. Li, Study on gasoline adsorptive desulfurization of resin-based modified spherical activated carbon, Shiyou Lianzhi Yu Huagong, 45 (2014) 10-15.
[45] R.L. Beatty, Microspheres containing metal carbide from metal-charged resin beads, DE2527093A1, 1976.
[46] L. Tosheva, J. Parmentier, S. Saadallah, C. Vix-Guterl, V. Valtchev, J. Patarin, Carbon and SiC Macroscopic Beads from Ion-Exchange Resin Templates, J. Am. Chem. Soc., 126 (2004) 13624-13625.
[47] A. Simonits, F. De Corte, J. Hoste, Single-comparator methods in reactor neutron activation analysis, J. Radioanal. Chem., 24 (1975) 31-46.

[48] M.A. Pimenta, G. Dresselhaus, M.S. Dresselhaus, L.G. Cancado, A. Jorio, R. Saito, Studying disorder in graphite-based systems by Raman spectroscopy, Phys. Chem. Chem. Phys., 9 (2007) 1276-1291.
[49] H. Kudielka, H. Rohde, Structural investigations of carbosulfides of titanium and zirconium, Z. Kristallogr., Kristallgeom., Kristallphys., Kristallchem., 114 (1960) 447-456.
[50] A. Bouhemadou, R. Khenata, Structural, electronic and elastic properties of M2SC (M=Ti, Zr, Hf) compounds, Phys. Lett. A, 372 (2008) 6448-6452.
[51] S.R. Kulkarni, N.A. Phatak, S.K. Saxena, Y. Fei, J. Hu, High pressure structural behavior and synthesis of Zr2SC, J. Phys.: Condens. Matter, 20 (2008) 135211/135211-135211/135216.
[52] M.F. Cover, O. Warschkow, M.M.M. Bilek, D.R. McKenzie, A comprehensive survey of M2AX phase elastic properties, J. Phys.: Condens. Matter, 21 (2009) 305403/305401-305403/305409.
[53] H. Fu, J. Yang, Z. Zhao, P. Feng, W. Liu, T. Gao, Static compressibility, thermal expansion and elastic anisotropy of Zr2SC single crystals, Solid State Commun., 149 (2009) 2110-2114.
[54] W. Feng, S. Cui, H. Hu, P. Feng, Z. Zheng, Y. Guo, Z. Gong, First-principles study on electronic structure and elastic properties of hexagonal Zr2SC, Phys. B (Amsterdam, Neth.), 405 (2010) 4294-4298.
[55] M.B. Kanoun, S. Goumri-Said, A.H. Reshak, A.E. Merad, Electro-structural correlations, elastic and optical properties among the nanolaminated ternary carbides Zr2AC, Solid State Sci., 12 (2010) 887-898.
[56] S. Cui, D. Wei, H. Hu, Z. Gong, Mechanical instability and ideal strengths of layered M2SC (M = Ti, Zr, and Hf) compounds, J. Appl. Phys. (Melville, NY, U. S.), 113 (2013) 083516/083511-083516/083517.
[57] M.T. Nasir, M.A. Hadi, S.H. Naqib, F. Parvin, A.K.M.A. Islam, M. Roknuzzaman, M.S. Ali, Zirconium metal-based MAX phases Zr2AC (A = Al, Si, P and S): A first-principles study, Int. J. Mod. Phys. B, 28 (2014) 1550022/1550021-1550022/1550016.
[58] A.C. Ferrari, Raman spectroscopy of graphene and graphite: Disorder, electron-phonon coupling, doping and nonadiabatic effects, Solid State Commun., 143 (2007) 47-57.
[59] R.E. Franklin, The structure of graphitic carbons, Acta Crystallogr., 4 (1951) 253-261.
[60] K.S.W. Sing, D.H. Everett, R.A.W. Haul, L. Moscou, R.A. Pierotti, J. Rouquerol, T. Siemieniewska, Reporting physisorption data for gas/solid systems, Pure Appl. Chem., 57 (1985) 603-619.
[61] G.L. Drisko, K.M. Chee, N. Scales, A. Ide, E. Sizgek, R.A. Caruso, V. Luca, One-pot preparation and uranyl adsorption properties of hierarchically porous zirconium titanium oxide beads using phase separation processes to vary macropore morphology, Langmuir, 26 (2010) 17581-17588.
[62] M.S.A. Rahaman, A.F. Ismail, A. Mustafa, A review of heat treatment on polyacrylonitrile fiber, Polymer Degradation and Stability, 92 (2007) 1421-1432.
[63] CRC Handbook of Chemistry and Physics, 96th ed., CRC Press, Boca Raton, 2015.
[64] C.F. Baes, R.E. Mesmer, The Hydrolysis of Cations, Robert E. Krieger Publishing Company, Inc, Malabar.
[65] M.D. Sacks, C.-A. Wang, Z. Yang, A. Jain, Carbothermal reduction synthesis of nanocrystalline zirconium carbide and hafnium carbide powders using solution-derived precursors, J. Mater. Sci., 39 (2004) 6057-6066.
[66] Q. Peng, J. Guo, Q. Zhang, J. Xiang, B. Liu, A. Zhou, R. Liu, Y. Tian, Unique lead adsorption behavior of activated hydroxyl group in two-dimensional titanium carbide, J Am Chem Soc, 136 (2014) 4113-4116.

762 [67] M. Ghidiu, J. Halim, S. Kota, D. Bish, Y. Gogotsi, M.W. Barsoum, Ion-Exchange and
763 Cation Solvation Reactions in Ti3C2 MXene, Chem. Mater., 28 (2016) 3507-3514.
764 [68] L. Wang, L. Yuan, K. Chen, Y. Zhang, Q. Deng, S. Du, Q. Huang, L. Zheng, J. Zhang,
765 Z. Chai, M.W. Barsoum, X. Wang, W. Shi, Loading Actinides in Multilayered Structures for
766 Nuclear Waste Treatment: The First Case Study of Uranium Capture with Vanadium Carbide
767 MXene, ACS Appl. Mater. Interfaces, 8 (2016) 16396-16403.
768 [69] Y. Ying, Y. Liu, X. Wang, Y. Mao, W. Cao, P. Hu, X. Peng, Two-Dimensional
769 Titanium Carbide for Efficiently Reductive Removal of Highly Toxic Chromium(VI) from
770 Water, ACS Appl. Mater. Interfaces, 7 (2015) 1795-1803.
771 [70] E.N. Hoffman, D.W. Vinson, R.L. Sindelar, D.J. Tallman, G. Kohse, M.W. Barsoum,
772 MAX phase carbides and nitrides: Properties for future nuclear power plant in-core
773 applications and neutron transmutation analysis, Nucl. Eng. Des., 244 (2012) 17-24.
774 [71] S. Zhao, J. Xue, Y. Wang, Q. Huang, Ab initio study of irradiation tolerance for different
775 Mn+1AXn phases: Ti3SiC2 and Ti3AlC2, J. Appl. Phys. (Melville, NY, U. S.), 115 (2014)
776 023503/023501-023503/023509.
777 [72] D.J. Tallman, E.N. Hoffman, E.a.N. Caspi, B.L. Garcia-Diaz, G. Kohse, R.L. Sindelar,
778 M.W. Barsoum, Effect of neutron irradiation on select MAX phases, Acta Mater., 85 (2015)
779 132-143.
780 [73] J. Xiao, T. Yang, C. Wang, J. Xue, Y. Wang, Investigations on Radiation Tolerance of
781 Mn+1AXn Phases: Study of Ti3SiC2, Ti3AlC2, Cr2AlC, Cr2GeC, Ti2AlC, and Ti2AlN, J.
782 Am. Ceram. Soc., 98 (2015) 1323-1331.
783 [74] C. Ang, C. Silva, C. Shih, T. Koyanagi, Y. Katoh, S.J. Zinkle, Anisotropic swelling and
784 microcracking of neutron irradiated Ti3AlC2-Ti5Al2C3 materials, Scr. Mater., 114 (2016)
785 74-78.
786 [75] D.J. Tallman, L. He, B.L. Garcia-Diaz, E.N. Hoffman, G. Kohse, R.L. Sindelar, M.W.
787 Barsoum, Effect of neutron irradiation on defect evolution in Ti3SiC2 and Ti2AlC, J. Nucl.
788 Mater., 468 (2016) 194-206.
789 [76] C. Ang, S. Zinkle, C. Shih, C. Silva, N. Cetiner, Y. Katoh, Phase stability, swelling,
790 microstructure and strength of Ti3SiC2-TiC ceramics after low dose neutron irradiation, J.
791 Nucl. Mater., 483 (2017) 44-53.
792 [77] D.J. Tallman, L. He, J. Gan, E.a.N. Caspi, E.N. Hoffman, M.W. Barsoum, Effects of
793 neutron irradiation of Ti3SiC2 and Ti3AlC2 in the 121-1085 °C temperature range, J. Nucl.
794 Mater., 484 (2017) 120-134.

795

796

Figures captions

Fig. 1. Optical microscopy image of ZrCX-1.

Fig. 2. (a) Powder XRD patterns. Key: h, hexagonal Zr_2SC; and (b) Raman spectra of ZrCX-1, representative of ZrCX-1 to -3.

Fig. 3. (a) and (b) SEM images of ZrCX-1 and ZrCX-2 internal fractured surfaces at lower magnification, respectively; (c) and (d) SEM images of the same at higher magnification; (e) nitrogen adsorption-desorption isotherms; and (f) pore size distributions.

Fig. 4. Structural evolution of ZrCX-1 with temperature. (a) Powder XRD patterns. Key: t, tetragonal ZrO_2; h, hexagonal Zr_2SC; (b) micropore, external and BET surface areas; and (c) in-plane carbon crystallite size.

Fig. 5. Adsorption data. (a) Adsorption pH dependence for ReO_4^- adsorption onto ZrCX-1 and a carbon blank; (b) isotherm data for ReO_4^- adsorption onto ZrCX-1 at pH 5 with fitted Langmuir and Freundlich models.

Fig. 6. STEM studies of Re-loaded ZrCX-1. (a) Bright field image; and corresponding STEM-EDS elemental maps (b–e) of Zr, S, O and Re distributions.

819

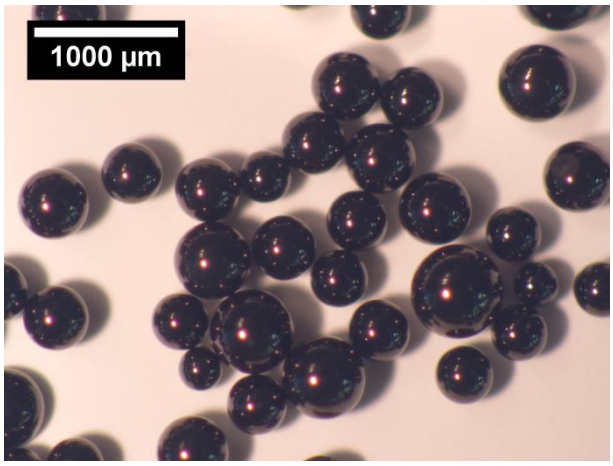

820

821 Fig. 1. Optical microscopy image of ZrCX-1.

822

823

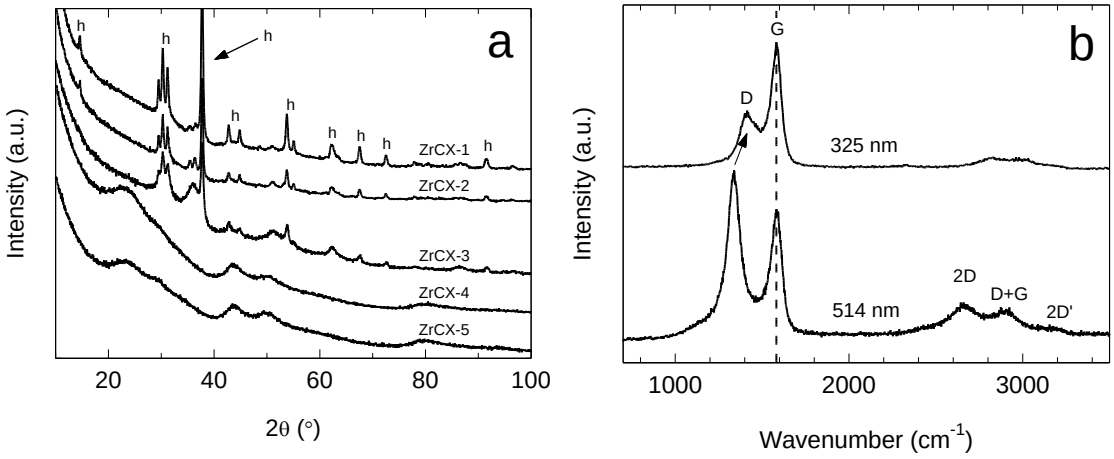

824

825 Fig. 2. (a) Powder XRD patterns. Key: t, tetragonal ZrO_2; h, hexagonal Zr_2SC; and (b) Raman

826 spectra of ZrCX-1, representative of ZrCX-1 to -3.

827

828

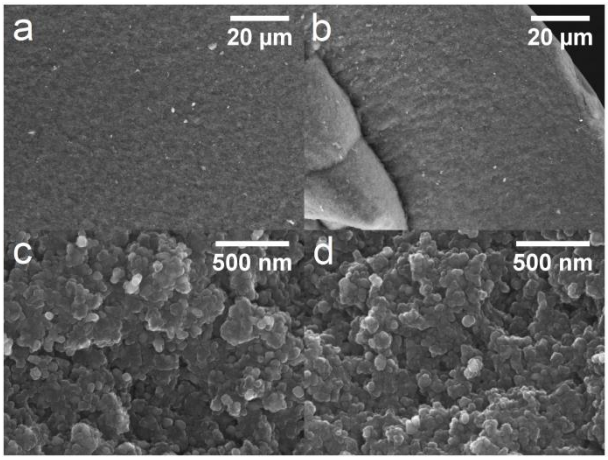

829

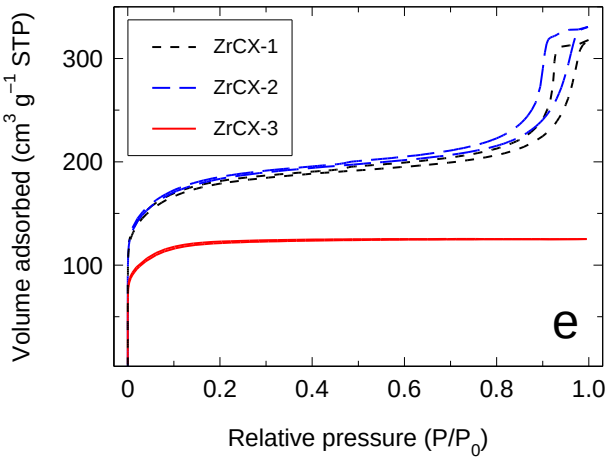

830

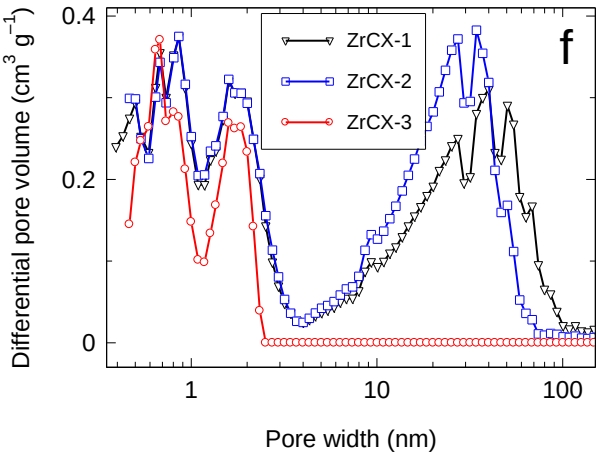

831 Fig. 3. (a) and (b) SEM images of ZrCX-1 and ZrCX-2 internal fractured surfaces at lower
832 magnification, respectively; (c) and (d) SEM images of the same at higher magnification; (e)
833 nitrogen adsorption-desorption isotherms; and (f) pore size distributions.

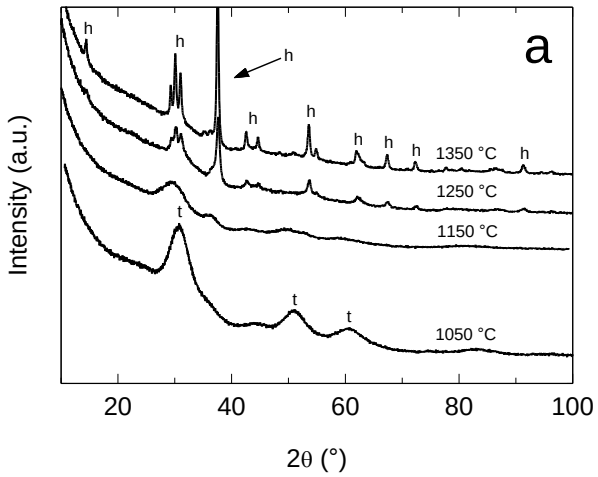

834

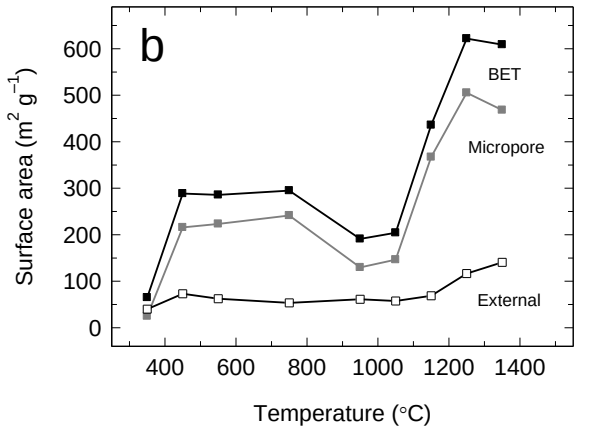

835

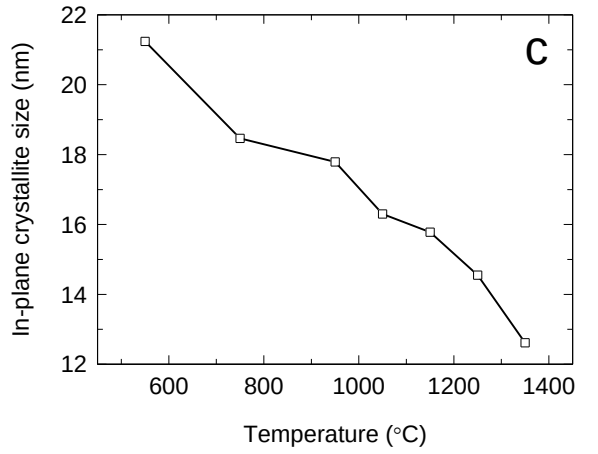

836

837 Fig. 4. Structural evolution of ZrCX-1 with temperature. (a) Powder XRD patterns. Key: t,
838 tetragonal ZrO_2; h, hexagonal Zr_2SC; (b) micropore, external and BET surface areas; and (c)
839 in-plane carbon crystallite size.

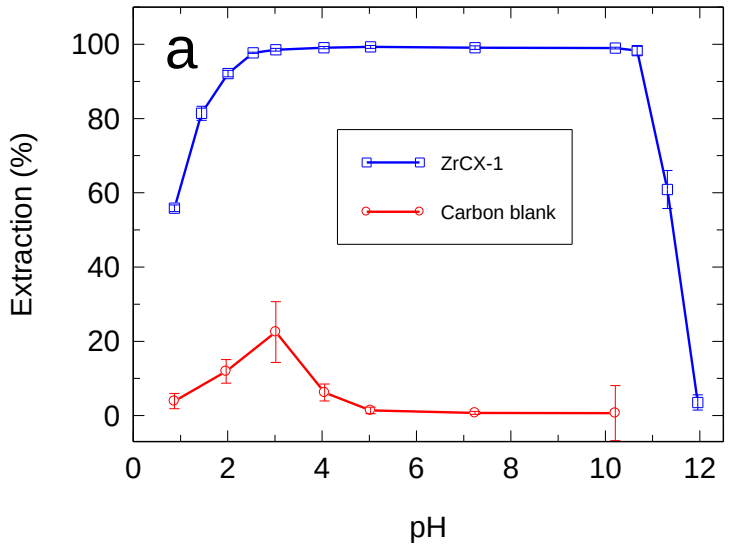

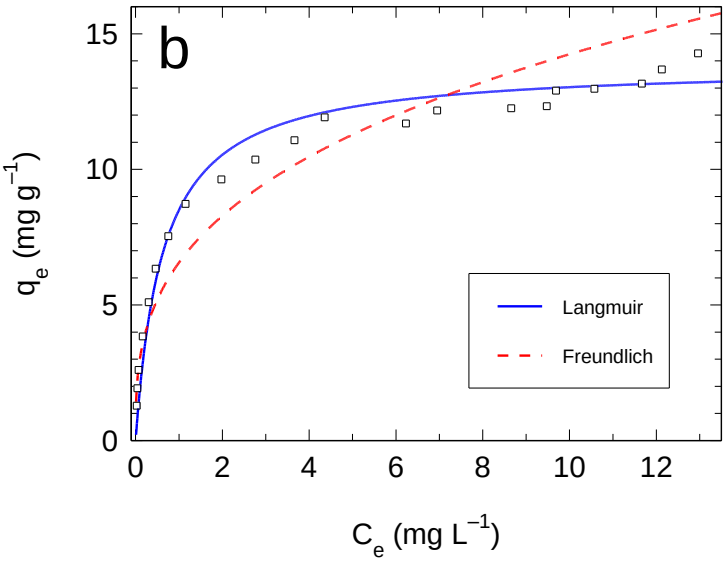

Fig. 5. Adsorption data. (a) Adsorption pH dependence for ReO_4^- adsorption onto ZrCX-1 and a carbon blank; (b) isotherm data for ReO_4^- adsorption onto ZrCX-1 at pH 5 with fitted Langmuir and Freundlich models.

847

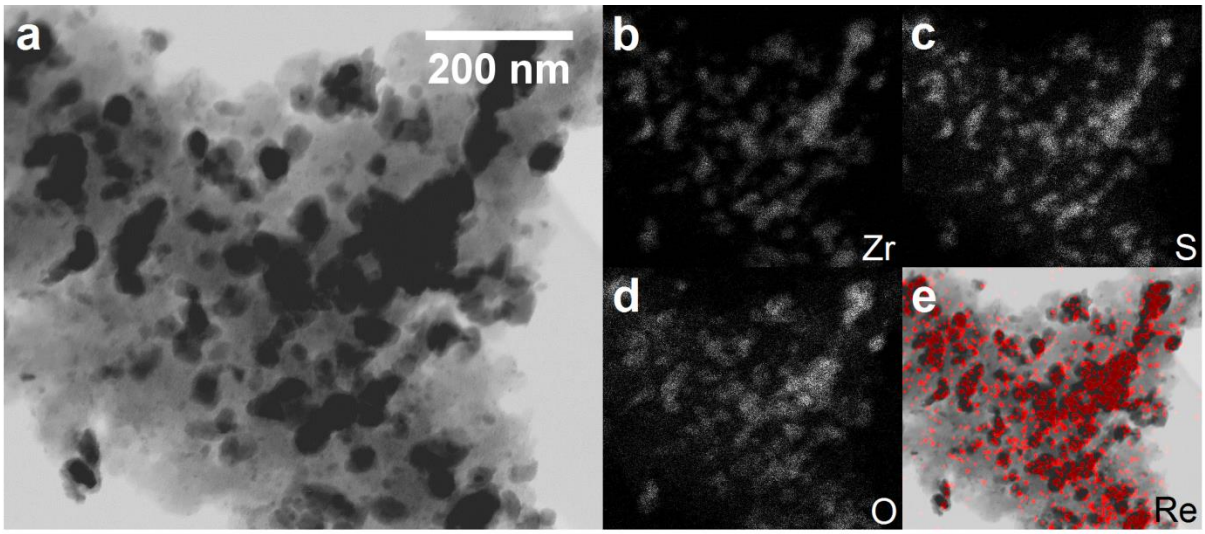

848

849 Fig. 6. STEM studies of Re-loaded ZrCX-1. (a) Bright field image; and corresponding

850 STEM-EDS elemental maps (c–e) of Zr, S, O and Re distributions.

851

852